Supplemental Information: Atmospheric Oxidation Impact on Sea Spray Produced Ice Nucleating Particles

Paul J. DeMott[a,*], Thomas C. J. Hill[1a], Kathryn A. Moore[a], Russell J. Perkins[a], Liora E. Mael[b,c], Heidi L. Busse[b,d], Hansol Lee[e], Chathuri P. Kaluarachchi[e], Kathryn J. Mayer[b,f], Jonathan S. Sauer[b], Brock Mitts[b], Alexei V. Tivanski[e], Vicki H. Grassian[b,g,h], Christopher D. Cappa[i], Timothy H. Bertram[j] and Kimberly A. Prather[b,g]

[a]*Department of Atmospheric Science, Colorado State University, Fort Collins, Colorado 80523, USA. E-mail: Paul.Demott@colostate.edu*
[b]*Department of Chemistry and Biochemistry, University of California, San Diego, La Jolla, California 92093, USA*
[c]*Department of Mechanical Engineering, University of Colorado, Boulder, CO, 80309, USA*
[d]*Department of Chemistry, The Pennsylvania State University, University Park, Pennsylvania 16802, USA*
[e]*Department of Chemistry, University of Iowa, Iowa City, Iowa 52242, USA*
[f]*Department of Chemistry, Colorado State University, Fort Collins, Colorado 80523, USA*
[g]*Scripps Institution of Oceanography, University of California, San Diego, La Jolla, California 92093, USA*
[h]*Department of Nanoengineering, University of California San Diego, La Jolla, California 92093, USA*
[i]*Department of Civil and Environmental Engineering, University of California, Davis, California 95616, USA*
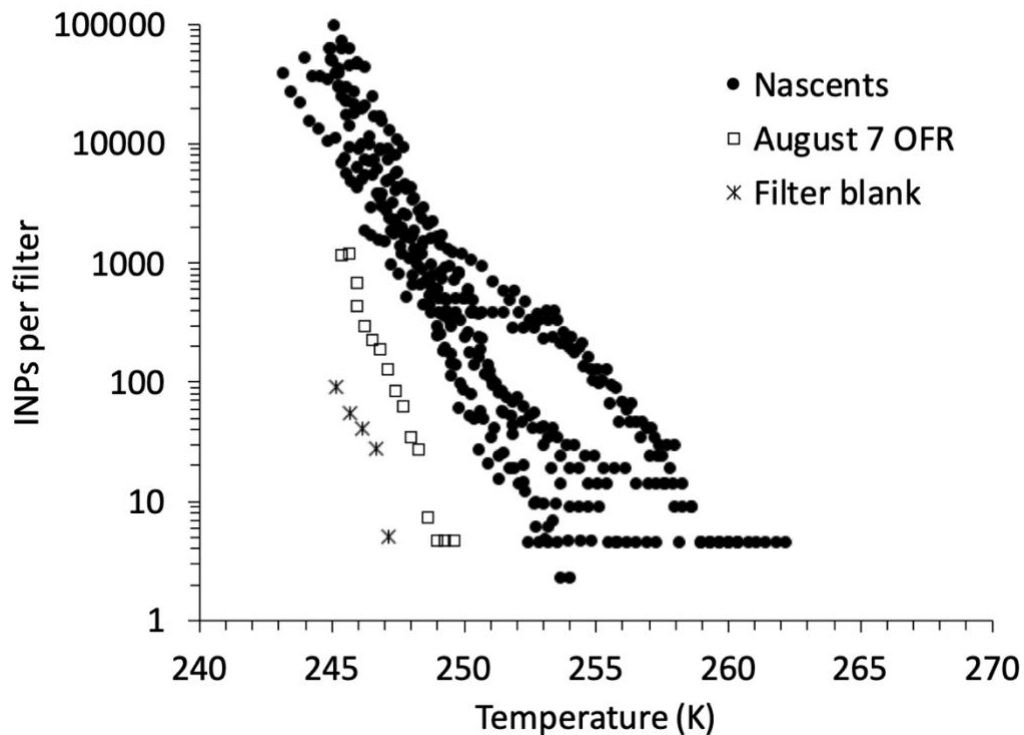[j]*Department of Chemistry, University of Wisconsin, Madison, Wisconsin 53706, USA*

Figure S1. INPs per filter versus temperature for all nascent SSA IS samples examined, one sample (August 7) where SSA from the wave channel passed through the OFR instrument with lamps active, and a filter blank that entailed opening a clean filter unit to flow of SSA through the OFR without lamps on for 3 minutes (15 liters). All experiments are already corrected for wells of DI suspension water freezing in each case.
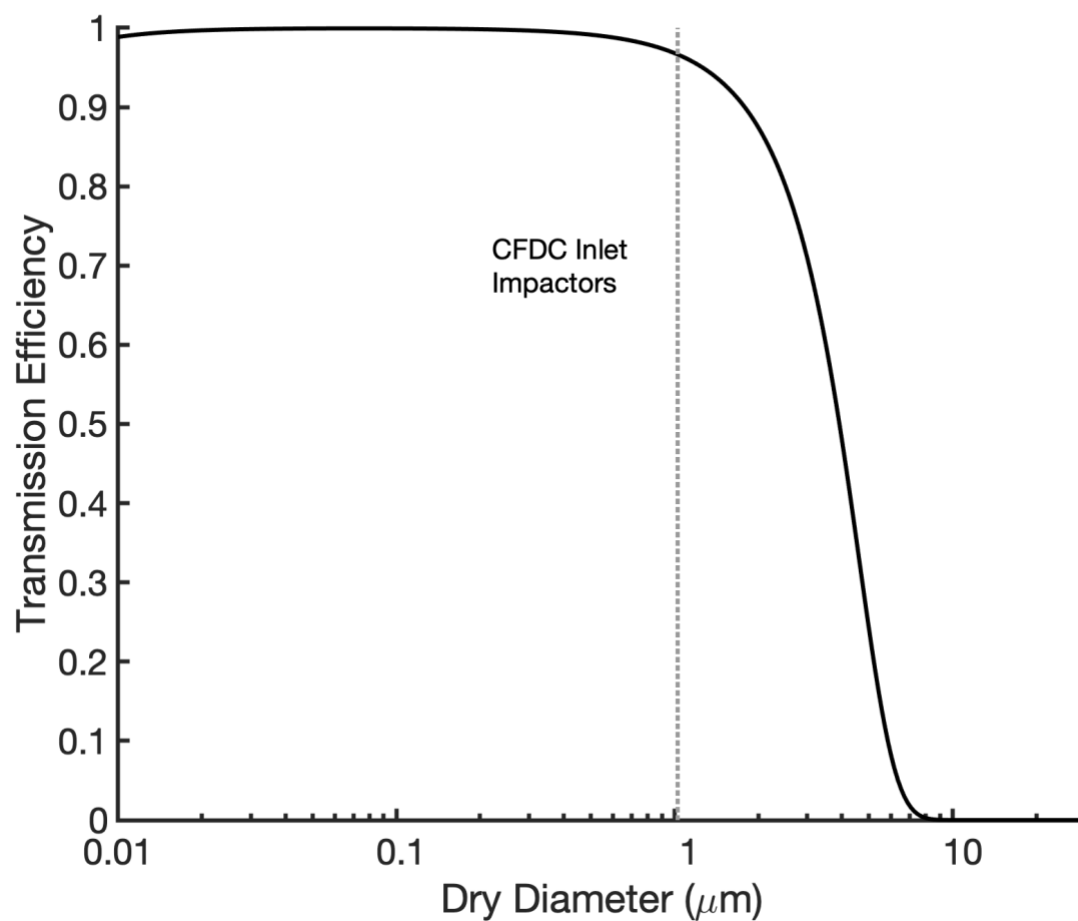
Figure S2. Line transmission losses for nascent line to the ice spectrometer filter.
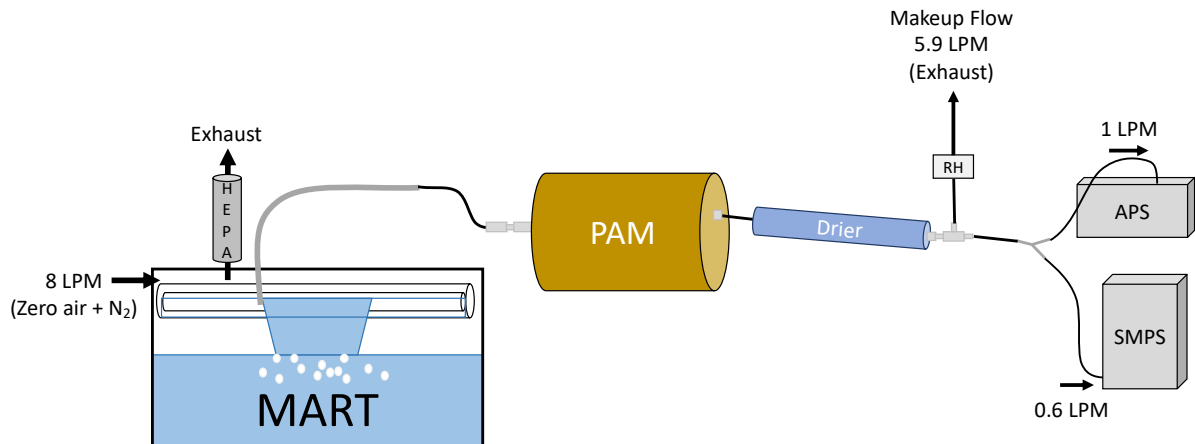
Figure S3. PAM aerosol transmission test set up using a MART tank. The tubing runs and sampling flow rates were set to mimic those present upstream of the MART in SeaSCAPE. The diffusion drier after the PAM was of sufficient residence time to reduce the relative humidity below 40%, which we will assume as dry conditions. The PAM was removed in experiments used to compare aerosol distributions measured by the SMPS and APS.
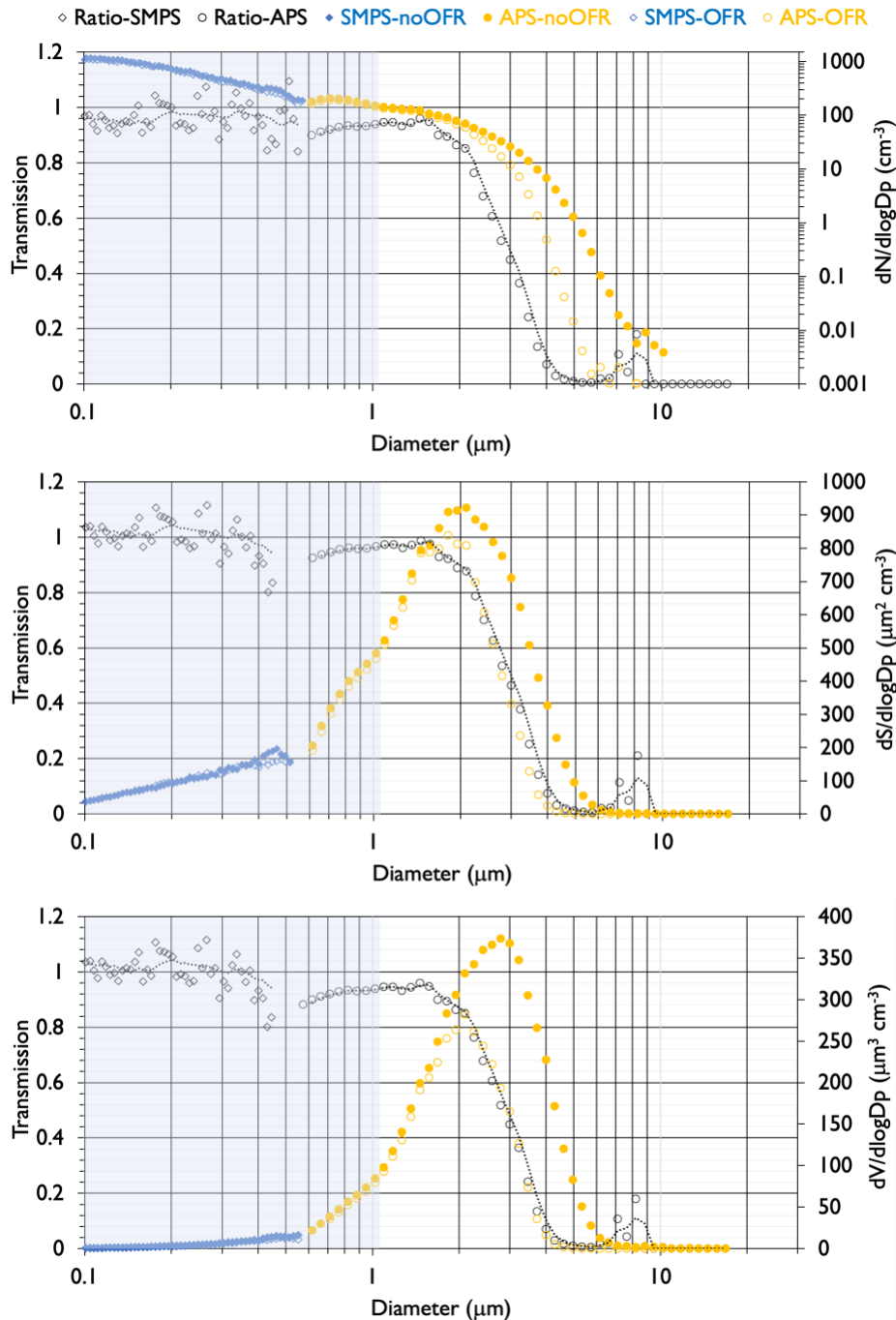
Figure S4. Aerosol distribution (SMPS in blue and APS in gold) on right scale and particle transmission factors (1 = no losses) represented as the ratio of counts on versus off passage through the OFR on the left scale versus equivalent spherical particle diameter in a) number, b) surface area, and c) volume space. Measurements with and without the PAM in series are indicated by filled and open symbols for number, surface area and volume by each instrument. Number concentrations are plotted on a logarithmic scale to also indicate the upper bound of particles sampled with and without the PAM. The shaded region denotes the physical size range of particles assessed with the CFDC instrument.
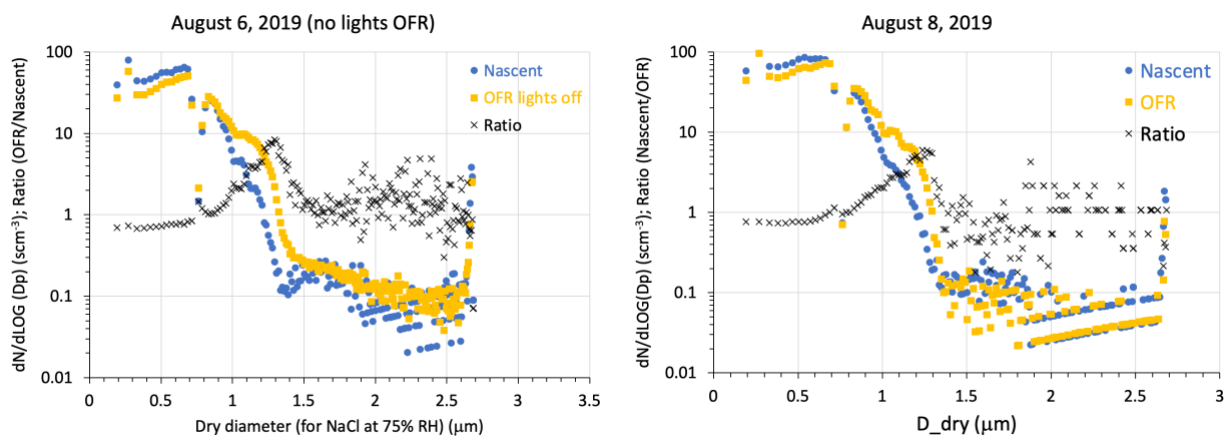
5

Figure S5. CFDC OPC size distributions for sampling the nascent versus OFR particle streams. These data align with the times of sampling shown in **Fig. 2** in the main manuscript. In both cases, potential size sorting effects are noted in passing air through the OFR occurring regardless of operation of the lamps. This is reflected by an enhancement of particles in a narrow size range from 1 to about 1.4 μm.
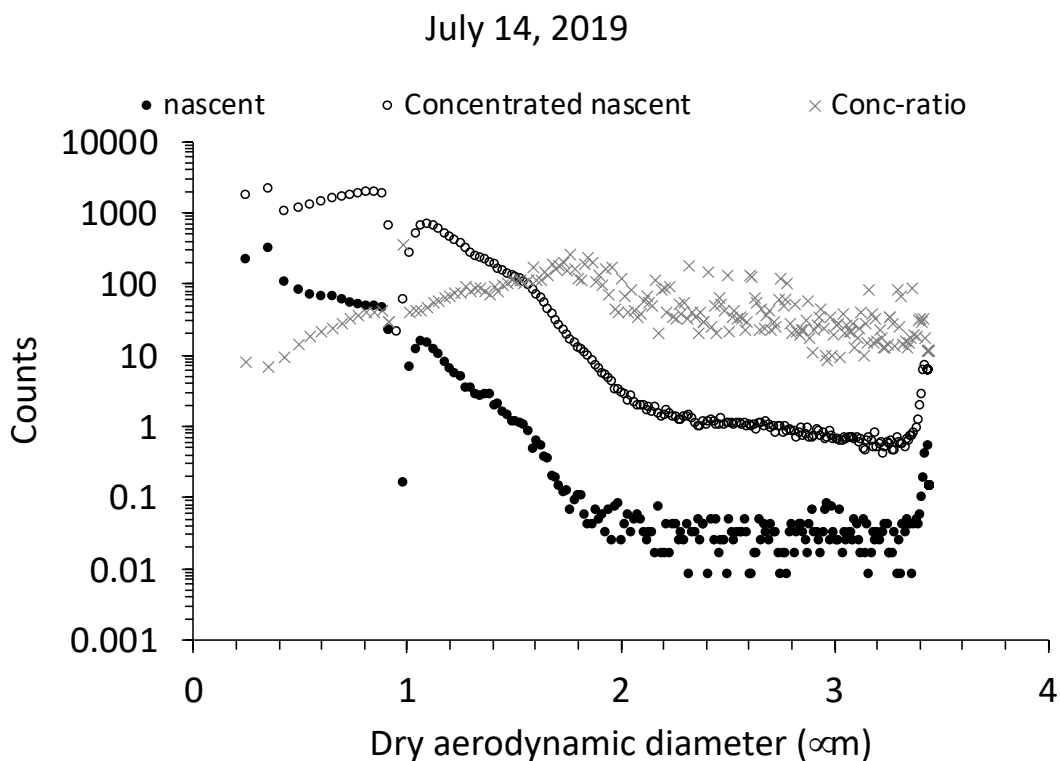

Figure S6. CFDC OPC size distribution showing unconcentrated and concentrated size distributions, and the concentration ratio (CF) calculated on the basis of these. A dry size of 1.5 μm is noted as the cut-point of the upstream CFDC impactors. This example is from bloom 2, just prior to the conduct of bloom 3 experiments reported in this paper.
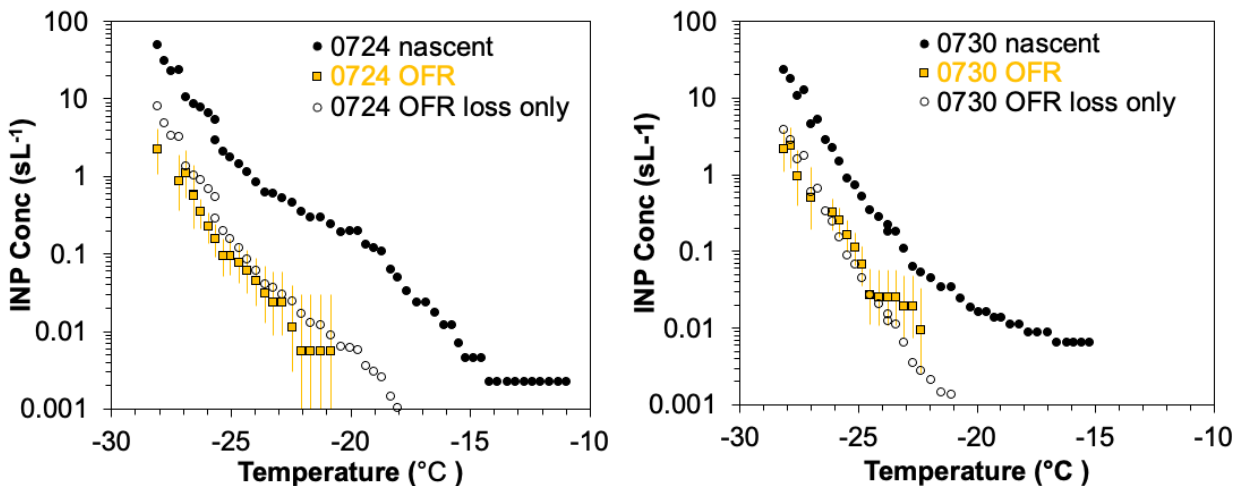
Figure S7. Two examples, in addition to Figure 3 of the main manuscript, of predicted physical losses of INPs in the OFR in comparison to the INP temperature spectra actually observed during OFR operation on the 24th or 30th of July, 2019.
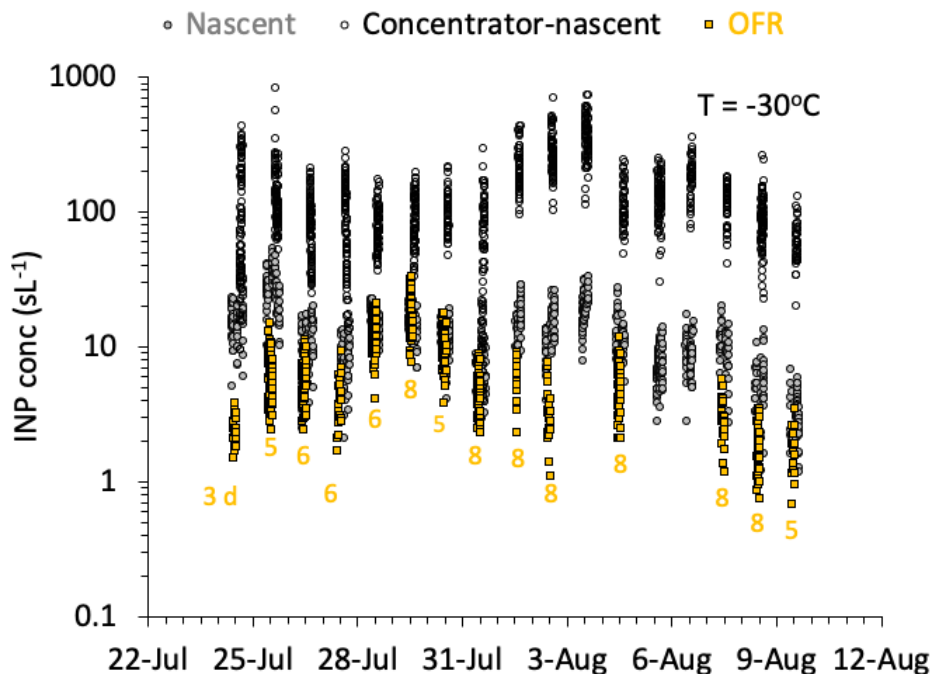

Figure S8. Non-averaged 1-min CFDC data (finest resolution processed for SeaSCAPE) for all bloom 3 measurement periods. Nascent data are given by filled circles (gray), nascent concentrated data by open circles (black) and OFR-processed data by yellow-filled squares. The numbers below each date are the equivalent days of aging using the OFR.
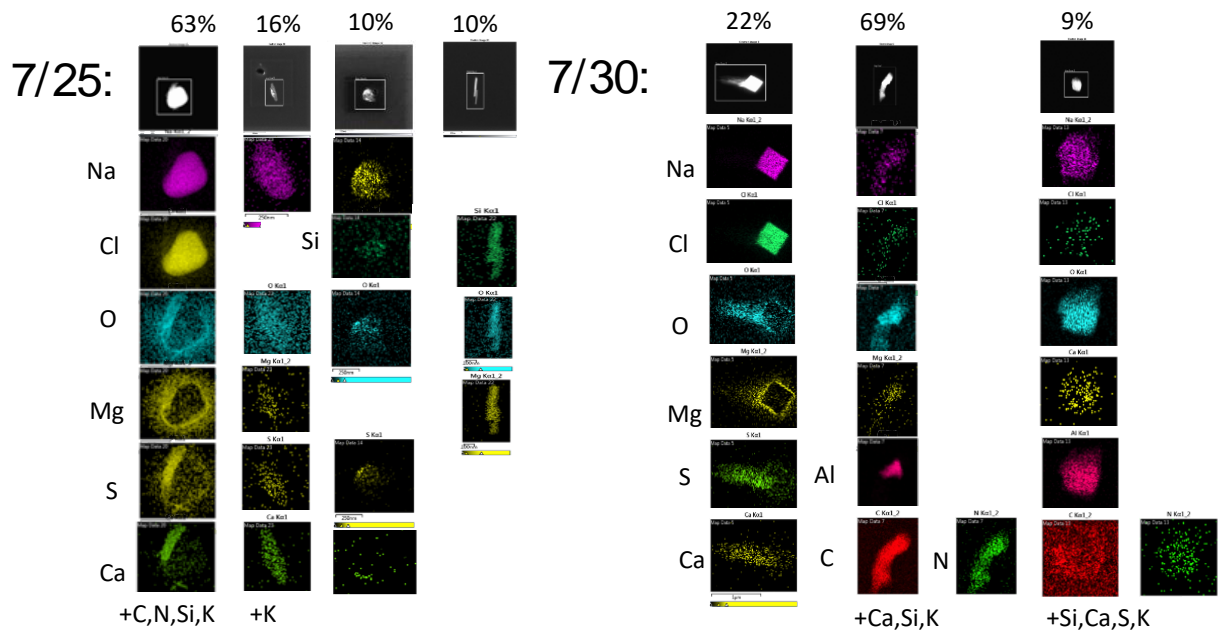
Figure S9. Mapping of elemental compositions in identified particle types, used as the basis of categorizing all particles in TEM samples for July 25 and July 30. Percentage values listed are the proportion of total analyzed particles in each morphological category on each day.

Micro-Raman model systems and use for spectral attribution of nascent and aged SSA. To aid in the analysis of SeaSCAPE samples, potential model systems were identified for analysis. Model chemical systems were prepared in bulk aqueous solutions and then, atomized, and deposited on a quartz substrate (Ted Pella Inc., no 1600-2) prepared with a hydrophobic coating (Rain-X). Following this procedure, the ice nucleation behavior and spectra were collected as described in Mael et al. (2019). Insoluble model systems were nebulized with a Meinhard TR-50 glass concentric nebulizer and sprayed onto hydrophobically coated quartz substrates. Particles deposited from (single and multi-component) solutions containing hexadecanol (98%, Sigma-Aldrich), palmitic acid (≥99%, Sigma-Aldrich), sodium alginate (≥99.5%, Sigma-Aldrich), benzene (99.8%, Sigma-Aldrich), N-acetylneuraminic (sialic) acid (97%, Sigma-Aldrich), laminarin (Alfa Aesar), lipopolysaccharide (LPS) (L4120, extracted from E. coli DIIILB4, purified by trichloroacetic acid extraction, Sigma-Aldrich), polydimethylsiloxane solution (Rain-X, ITW

Global Brands, Houston, TX, USA), black carbon, hydroquinone (≥99%, Sigma-Aldrich), NaCl (99%, Fischer Scientific), glucose (99% Sigma-Aldrich), sucrose (≥99%, Sigma-Aldrich), nonanoic acid (≥97%, Sigma-Aldrich), L-phenylalanine (≥98%, Sigma-Aldrich), L-tryptophan (≥98%, Sigma-Aldrich), and L-tyrosine (≥98%, Sigma-Aldrich).

Nascent and aged INP spectra are assembled in **Figures S10 and S11**. These spectra are accompanied by tables which indicate on which dates these spectra were collected, how many particles corresponded to each spectrum. We also reiterate that 250 K was a considered as a temperature above which there were no artifactual secondary freezing due to the ice growth of adjacent droplets on substrates following cooling. The three types of spectra found across multiple samples, indicated by #1, #2 and #3, for low signal, siliceous and soot are discussed in the main manuscript. Additional spectra found across multiple days were florescence spectra, spectrum #4 in **Fig. S10**, characterized by Raman spectra that increase rapidly and plateaus across the wavenumber range investigated (with regular breaks in signal corresponding to the wavenumbers where the grating shifts during the collection of a spectrum). Hydrates were also seen across multiple dates, including spectra #05, 06, 18, and 24, characterized by the presence of the O-H stretching band between 3200 cm^{-1} and 3500 cm^{-1}. Also shown in **Figures S10** and **S11**, are unique spectra only seen once throughout the bloom as well as spectra unique to a particular date during the bloom (and measured across that particular substrate).

Other interesting spectra freezing at "warm" temperatures on the cold stage include spectrum #20 from the 08-04-19 nascent substrate (**Fig. S11**). Two of the seven spectra/particles associated with spectrum #20 refroze at >250 K, and these are shown in **Fig. S12**. Interestingly, the spectra of these two particles are nearly identical, but one froze at 260.6 K while the other froze at 250.0 K. When compared to model systems, these two particles are in good agreement with the model

fatty acid and alcohol, palmitic acid and hexadecanol, which are not spectrally distinguishable with Raman spectroscopy. Fatty acids and alcohols have been observed previously in other field studies and are known to be present in SSA (Cochran et al., 2017). Despite the spectral similarity, the different ice nucleating abilities distinguish the two samples. The ca. 10-degree difference in IN onset temperature agrees with the difference in ice nucleation onset temperatures of the alcohol and acid observed by Perkins et al. (2020). The ice nucleation temperatures of palmitic acid and hexadecanol model systems, 260 and 250 K, respectively, agree with the ice nucleation temperatures measured in the SeaSCAPE SSA samples. Although there is excellent agreement with the fatty acid/alcohol model systems, both spectra contain a small peak at 3063 cm^{-1} which would indicate some unsaturation within the sample. This may be a result of another molecule or compound present with the larger particle, as these are not pure samples generated within the lab. Similar spectral signatures (with the 3063 cm^{-1} peak) have been seen by Deng et al. (2016) in SSA and have been identified as long chain aliphatics. Five other particles represented by spectrum #20 (and as such are most likely fatty acids or alcohols) did not freeze warmer than 250 K. This would indicate that there may be other molecules present which are suppressing ice nucleation, most likely NaCl (Perkins et al., 2020). As NaCl is Raman inactive, it is difficult to quantify the relative concentration NaCl associated with each spectrum. However, further study of the ice nucleation of fatty acid and/or alcohol systems with varying concentrations of NaCl may elucidate a relationship between concentration and ice nucleation onset temperature and provide a way to characterize the amount of NaCl associated with these particles.

The remaining particles that froze warmer than 250 K were unique spectra, which only appear once within ice residuals isolated from the CFDC, highlighted in **Fig. S13**. Comparison to spectra of individual amino acids and polypeptides suggests that these samples contain biological material,

in particular L-phenylalanine, L-tyrosine, and L-tryptophan (**Fig. S13**) (Zhu et al., 2011). As amino acids on their own are not particularly strong INP, we suspect that these particles were components of larger biological systems, most likely longer chain peptides, which have been shown to be INPs (Duman et al., 2001; O'Sullivan et al., 2016; Wu et al., 2009; Pandey et al., 2016). It may be that the particular amino acids noted here contribute more to the Raman signature than the other components of the protein, bacteria or biological system. Because both spectra and ice nucleating temperatures of these particles were measured, these samples will act as a reference for future work characterizing the ice nucleation ability of marine samples.
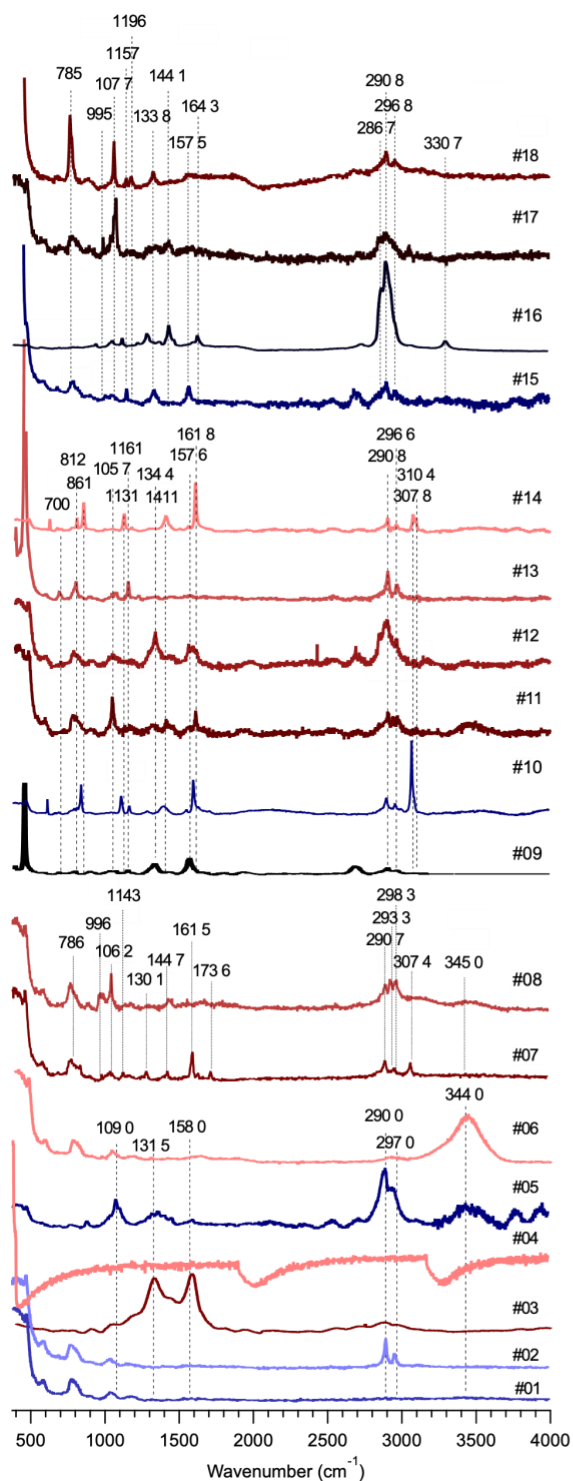
Spectrum	Date(s) collected	Number of corresponding particles	# of particles freezing warmer than 250 K
#18	07-31-19N	1	-
#17	07-31-19N	1	-
#16	07-31-19N	1	1
#15	07-31-19N	1	-
#14	07-28-19 OFR	7	1
#13	07-28-19 OFR	1	-
#12	07-28-19 OFR	1	-
#11	07-28-19 OFR	1	-
#10	07-28-19 OFR	1	1
#09	07-28-19 OFR	1	-
#08	07-28-19N	2	-
#07	07-28-19N	1	-
#06	07-26-19N; 07-28-19 N	18	-
#05	07-26-19N	1	-
#04	07-28-19N; 07-28-19 OFR; 07-31-19 N; 08-04-19 OFR	8	--
#03	07-26-19N; 07-28-19 N; 07-28-19 OFR; 08-08-19 OFR	16	6
#02	07-26-19N; 07-28-19 N; 07-28-19 OFR; 07-31-19 N; 08-04-19 N; 08-04-19 OFR; 08-08-19 OFR	91	3
#01	07-26-19N; 07-28-19 N; 07-28-19 OFR; 07-31-19 N; 08-04-19 N; 08-04-19 OFR; 08-08-19 OFR	132	38

Figure S10. Representative spectra collected from a survey of the ice residual particles collected from the CFDC, the date each representative spectrum was found, the total number of spectra corresponding to each representative spectrum, and the number of particles, if any, that froze warmer than 250 K.

Figure S11. Continued from Figure S8, representative spectra collected from a survey of the ice residual particles collected from the CFDC, the date each representative spectrum was found, the total number of spectra corresponding to each representative spectrum, and the number of particles, if any, that froze warmer than 250 K.
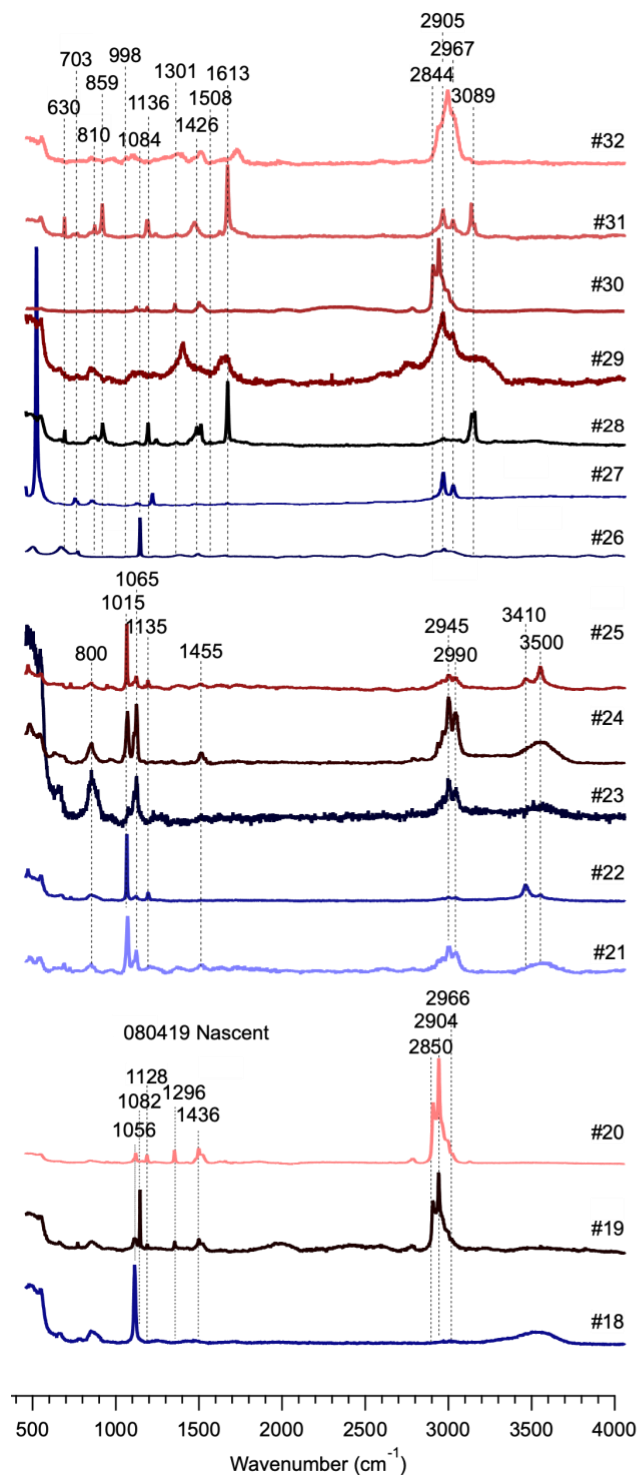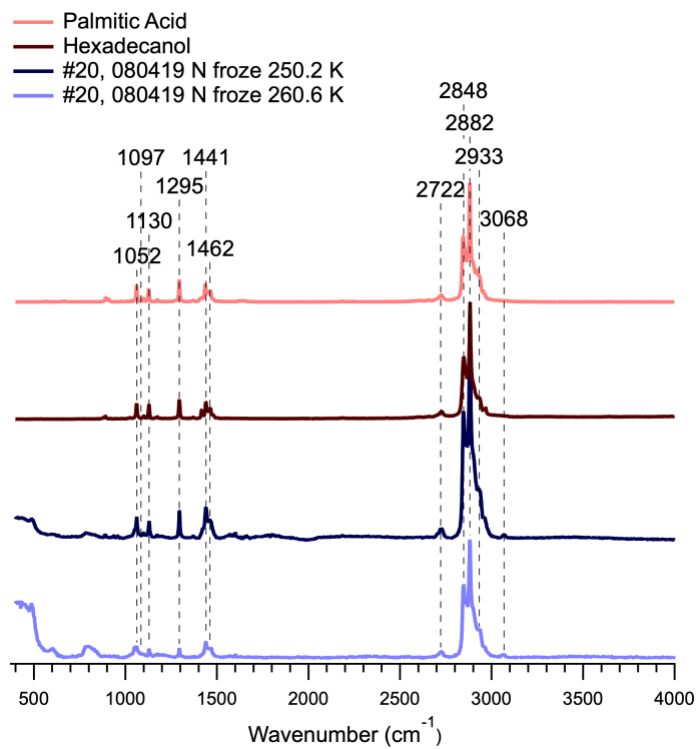
Spectrum	Date(s) collected	Number of corresponding particles	# of particles freezing warmer than 250 K
#32	08-08-19 OFR	4	
#31	08-08-19 OFR	16	
#30	08-08-19 OFR	2	
#29	08-08-19 OFR	2	
#28	08-08-19 OFR	1	
#27	08-08-19 OFR	1	
#26	08-08-19 OFR	1	
#25	08-04-19 OFR	1	
#24	08-04-19 OFR	1	
#23	08-04-19 OFR	4	
#22	08-04-19 OFR	14	
#21	08-04-19 OFR	21	
#20	08-04-19 N	7	2
#19	08-04-19 N	1	
#18	08-04-19 N	1	

Figure S12. Raman spectra of two CDFC isolated ice residuals that froze at 250.2 K and 260.6 K as well as model system spectra of palmitic acid and hexadecanol.
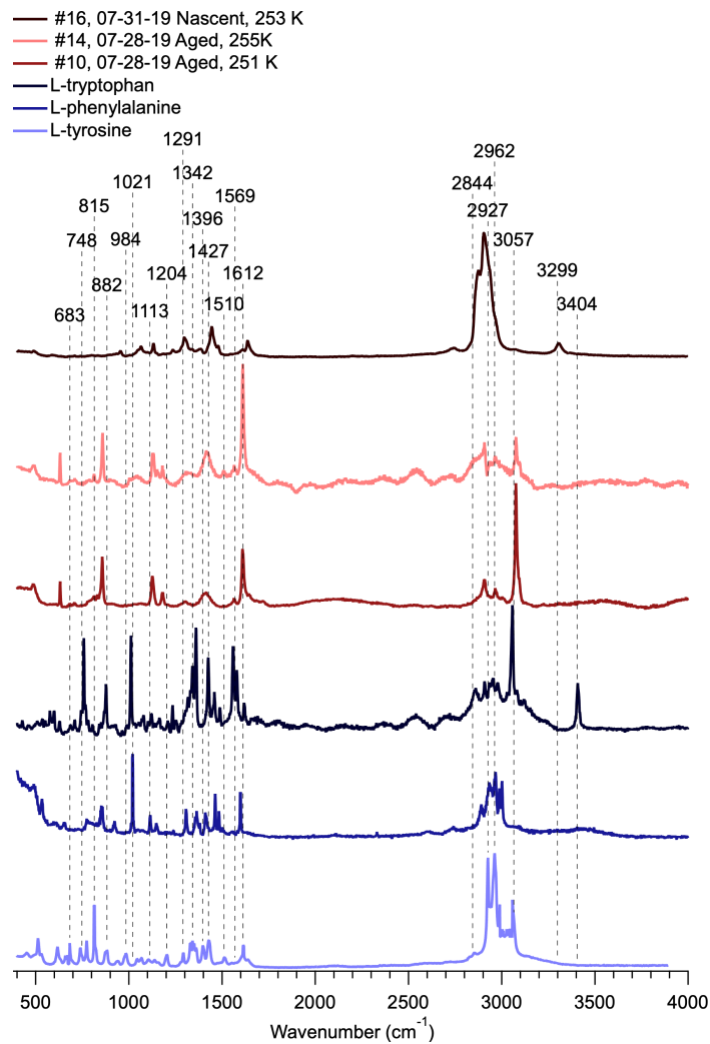
Figure S13. Unique Raman spectra of three particles that froze warmer than 250 K with Raman spectra of three model amino acids, L-tryptophan, L-phenylalanine, and L-tyrosine.
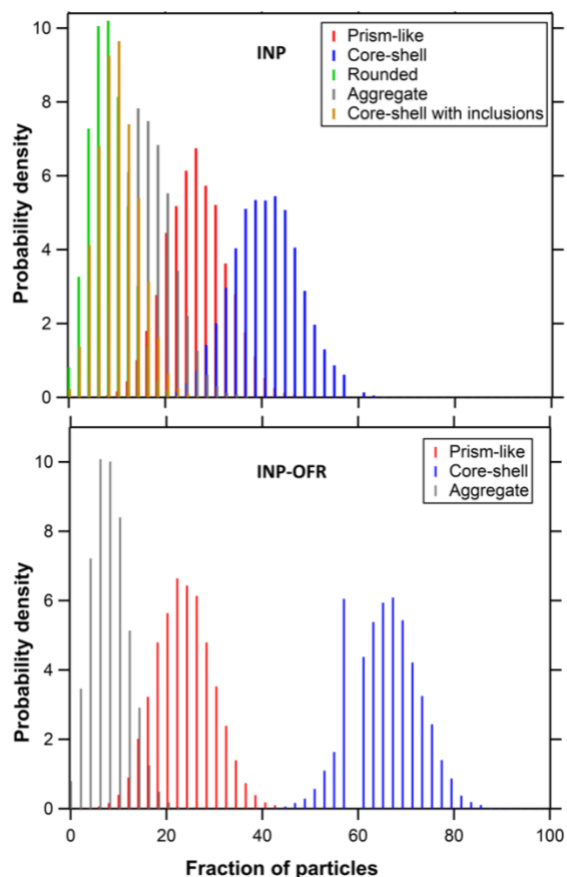
Figure S14. The statistical probability distribution of main morphological categories (prism-like, core-shell, rounded, aggregate, and core-shell with inclusions) for INPs (based on the measurements of 50 particles), and OFR INPs (based on the measurements of 50 particles) following AFM analysis. Based on the analysis, for both INP and INP-OFR, the probability of obtaining core-shell particles was significantly different from other morphologies. Additionally, the fraction of core-shell particles from INP-OFR was larger and significantly different from the nascent INP. This confirms the conclusion that observed increase in the relative abundance of core-shell morphology in INP-OFR sample is a "true" statistically significant observation despite of the finite number of particles studied here for each sample.
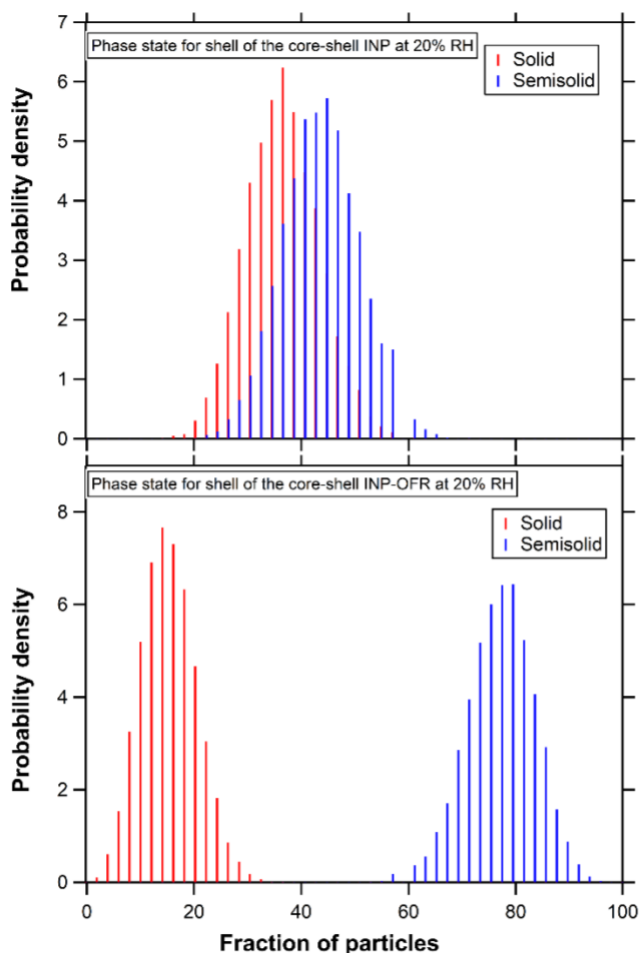
Figure S15. The statistical probability distribution of solid and semisolid phase states for shell region of core-shell INPs (based on the measurements of 11 particles), and OFR INPs (based on the measurements of 30 particles) following AFM analysis. Based on the analysis, probability of obtaining core-shell particles with either solid or semisolid shells are similar for nascent INPs, while statistically and significantly different for INP-OFR. Additionally, INP-OFR had a higher fraction of core-shells at semisolid phase state and lower fraction of core-shell at solid phase state, compared to INP.

References

R. E. Cochran, O. Laskina, J. V. Trueblood, A. D. Estillore, H. S. Morris, T. Jayarathne, C. M. Sultana, C. Lee, P. Lin, J. Laskin, A. Laskin, J A. Dowling, Z. Qin, C. D. Cappa, T. H. Bertram, A. V. Tivanski, E. A. Stone, K. A. Prather, and V. H. Grassian, Molecular Diversity of Sea Spray Aerosol Particles: Impact of Ocean Biology on Particle Composition and Hygroscopicity. *Chem* 2017, https://doi.org/10.1016/j.chempr.2017.03.007, **2** (5), 655–667.

C. Deng, S. D. Brooks, G. Vidaurre, and D. C. O. Thornton, Using Raman Microspectroscopy to Determine Chemical Composition and Mixing State of Airborne Marine Aerosols over the

Pacific Ocean. *Aerosol Science and Technology,* 2014, https://doi.org/10.1080/02786826.2013.867297, **48** (2), 193–206.

J. G. Duman, Antifreeze and Ice Nucleator Proteins in Terrestrial Arthropods. *Annu. Rev. Physiol.* 2001, https://doi.org/10.1146/annurev.physiol.63.1.327, **63** (1), 327–357.

L. E. Mael, H. Busse and V. H. Grassian, Measurements of Immersion Freezing and Heterogeneous Chemistry of Atmospherically Relevant Single Particles with Micro- Raman Spectroscopy, *Analytical Chemistry*, 2019, https://doi.org/10.1021/acs.analchem.9b01819, **91**, 11138−11145.

C. S. McCluskey, C. S., T. C. J. Hill, C. M. Sultana, O. Laskina, J. Trueblood, M. V. Santander, C. M. Beall, J. M. Michaud, S. M Kreidenweis, K. A. Prather, V. H. Grassian, and P. J. DeMott, A mesocosm double feature: Insights into the chemical make-up of marine ice nucleating particles, *J. Atmos. Sci*., 2018, https://doi.org/10.1175/JAS-D-17-0155.1, **75**, 2405-2423.

D. O'Sullivan, B. J. Murray, J. F. Ross, and M. E. Webb, The Adsorption of Fungal Ice-Nucleating Proteins on Mineral Dusts: A Terrestrial Reservoir of Atmospheric Ice-Nucleating Particles. *Atmospheric Chemistry and Physics* 2016, https://doi.org/10.5194/acp-16-7879-2016, **16** (12), 7879–7887.

R. Pandey, K. Usui, R. A. Livingstone, S. A. Fischer, J. Pfaendtner, E. H. G. Backus, Y. Nagata, J. Fröhlich-Nowoisky, L. Schmüser, S. Mauri, J. F. Scheel, D. A. Knopf, U. Pöschl, M. Bonn, and T. Weidner, Ice-Nucleating Bacteria Control the Order and Dynamics of Interfacial Water. *Science Advances*, 2016, https://doi.org/10.1126/sciadv.1501630, **2** (4).

R. J. Perkins, M. G. Vazquez de Vasquez, E. E. Beasley, T. C. J. Hill, E. A. Stone, H. C. Allen, and P. J. DeMott, Relating Structure and Ice Nucleation of Mixed Surfactant Systems Relevant to Sea Spray Aerosol. *J. Phys. Chem. A* 2020, https://doi.org/10.1021/acs.jpca.0c05849, **124** (42), 8806–8821.

Z. Wu, L. Qin, and V. K. Walker,. Characterization and Recombinant Expression of a Divergent Ice Nucleation Protein from "Pseudomonas Borealis." *Microbiology,* 2009, https://doi.org/10.1099/mic.0.025114-0, **155** (4), 1164–1169.

G. Zhu, X. Zhu, Q. Fan, and X. Wan, Raman Spectra of Amino Acids and Their Aqueous Solutions. *Spectrochimica Acta - Part A: Molecular and Biomolecular Spectroscopy,* 2011, https://doi.org/10.1016/j.saa.2010.12.079, **78** (3), 1187–1195.